Near 6-GHz Sezawa Mode Surface Acoustic Wave Resonators Using AlScN on SiC

Xingyu Du[®], Graduate Student Member, IEEE, Nishant Sharma[®], Zichen Tang[®], Member, IEEE, Chloe Leblanc[®], Deep Jariwala[®], Senior Member, IEEE, and Roy H. Olsson III[®], Senior Member, IEEE

Abstract-Surface Acoustic Wave (SAW) devices featuring Aluminum Scandium Nitride (AlScN) on a 4H-Silicon Carbide (SiC) substrate, offer a unique blend of high sound velocity, low thermal resistance, substantial piezoelectric response, simplified fabrication, as well as suitability for high-temperature and harsh environment operation. This study presents high-frequency SAW resonators employing AlScN thin films on SiC substrates, utilizing the second SAW mode (referred to as the Sezawa mode). The resonators achieve remarkable performance, boasting a K² value of 5.5% at 4.7 GHz and a maximum Bode-O (Omax) of 911 at 4.3 GHz, outperforming previous AlScN SAW devices. Additionally, a SAW resonator with a 0.96 μ m wavelength attains 5.9 GHz frequency with K^2 of 4.0% and Q_{max} of 762. Our study underscores the potential of the AlScN on SiC platform for advanced radio-frequency applications. [2024-0075]

Index Terms—Surface acoustic wave, AlScN, SiC, microelectromechanical systems, acoustic device.

I. Introduction

COUSTIC wave devices have established their dominance in high-volume, radio frequency (RF) front-end signal processing applications. Their superiority arises from impressive performance metrics, encompassing compact size, minimal insertion loss, high isolation, low power consumption, precise filter responses, and potential for integration and co-fabrication alongside analog and RF electronics [1]. In order to meet the stringent requirements of upcoming wireless standards, the next generation of surface- and bulk-acoustic wave (SAW and BAW) resonators must exhibit an exceptionally sharp spectral response which translates to both a high-quality factor (Q-factor) and a high electromechanical coupling coefficient (K²) [2]. These attributes necessitate low propagation loss and a wider bandwidth, crucial for the performance of acoustic filters.

Manuscript received 19 April 2024; revised 14 July 2024; accepted 15 July 2024. Date of publication 31 July 2024; date of current version 3 October 2024. This work was supported in part by the Defense Advanced Research Projects Agency (DARPA) Traveling-Wave Energy Enhancement Devices (TWEED) Program under Award HR0011-21-9-0055 and in part by NSF CAREER Award under Grant 1944248. This work was carried out in part at the Singh Center for Nanotechnology at the University of Pennsylvania, a member of the National Nanotechnology Coordinated Infrastructure (NNCI) network, which is supported by the National Science Foundation (Grant No. HR0011-21-9-0004). Subject Editor R. Lu. (Corresponding author: Roy H. Olsson III.)

The authors are with the Department of Electrical and Systems Engineering, University of Pennsylvania, Philadelphia, PA 19104 USA (e-mail: rolsson@seas.upenn.edu).

Color versions of one or more figures in this article are available at https://doi.org/10.1109/JMEMS.2024.3430984.

Digital Object Identifier 10.1109/JMEMS.2024.3430984

SAW filters have been widely used in mobile phone handsets at frequencies up to 2 GHz due to their ease of fabrication, cost-effectiveness, and high repeatability [3]. However, achieving practical SAW devices operating at higher frequencies, such as 4 to 6 GHz, poses significant challenges, making it difficult for them to compete with their BAW counterparts [2], [4]. At these frequencies, the miniaturization of the interdigital transducers (IDTs) limits mass production, while other factors such as increased series resistance of the IDTs, reduced reliability due to poor heat dissipation and high thermal stress constrain their overall performance. Overcoming this frequency constraint involves leveraging high-velocity acoustic waves, leading to extensive research on acoustic wave devices operating above 3 GHz, making use of high-velocity SAW [5], [6], [7], [8], [9].

Piezoelectric materials placed on silicon carbide (SiC) have previously demonstrated SAWs with significantly higher acoustic velocity compared to those on silicon, reaching values exceeding ~ 6600 m/s [10], 6310 m/s [9], and >10,000 m/s [11] for the second order SAW mode (referred to as the Sezawa mode) [9]. This characteristic enables higher-frequency operation of SAW filters while effectively confining the acoustic wave energy near the SiC surface. SiC has also gained prominence in power electronics and high-temperature electronics due to its high thermal conductivity of 370 W/(m·K), which enhances the capability of SiC-based SAW filters to handle higher power levels before signal compression [12], [13], [14]. Additionally, SiC offers the advantage of a close lattice match with Aluminum Nitride (AIN) facilitating the growth of high-quality, crystalline c-axis oriented piezoelectric thin films [10], [15], [16], [17]. This feature simplifies the integration of piezoelectric materials with substrates at wafer scale.

Through alloying of Scandium (Sc) with Aluminum Nitride (AlN), previous studies have demonstrated a notable enhancement in the electromechanical coupling coefficient. The piezoelectric response coefficient for AlScN maximizes at around 42% Scandium concentration. Comparing Al_{0.58}Sc_{0.42}N with pure AlN, the piezoelectric charge coefficient d₃₃ is 4 times and the transverse piezoelectric coefficient, d₃₁, is about 6 times higher [18], [19]. It is important to note that the coupling is also inversely proportional to the relative dielectric constant and directly proportional to the material's modulus. The relative dielectric constant increases and modulus decreases slightly with increasing scandium

1057-7157 © 2024 IEEE. Personal use is permitted, but republication/redistribution requires IEEE permission. See https://www.ieee.org/publications/rights/index.html for more information.

concentration [20]. As a result, the overall coupling coefficient does not experience a quadratic growth with respect to the scandium concentration but is still significantly higher than that at lower Scandium concentrations [21].

In addition, high quality AlScN can be grown via sputtering at temperatures below 400 °C at lower cost and higher growth rates than epitaxial growth methods [17].

This study presents SAW resonators using ~ 0.8 um thick, Al_{0.58}Sc_{0.42}N thin films on SiC substrates, achieving a K² up to 5.5% at 4.7 GHz and a maximum Bode-Q (Q_{max}) [22] of 911 at 4.3 GHz, surpassing previous works. The resonators exhibited a maximum Figure of Merit (FoM) of 31 at 4.7 GHz, doubling previous reports on AlScN based SAW resonators [6], [9], [11], [23]. Notably, a 0.96 μ m wavelength SAW resonator device reached a frequency of 5.9 GHz while maintaining high K² of 4.0% and Q_{max} of 762. We study the frequency scaling of AlScN/SiC SAW devices by fabricating and comparing SAW resonator devices with different wavelengths.

II. FABRICATION PROCESS

The fabrication of the AlScN devices adhered to the process flow depicted in Fig. 1(a). Four-inch, high resistivity (> 10⁵ ohm·cm) 4H-SiC substrates from Xiamen Powerway Advanced Material Co., Ltd were employed. Piezoelectric thin films were sputter deposited without breaking vacuum using an Evatec CLUSTERLINE 200 II PVD system at a temperature of 350 °C and a base pressure below 1×10^{-7} mbar. The deposition process consisted of three steps: a 15 nm AlN seed layer, a 35 nm gradient layer, and a 780 nm bulk AlScN layer. As demonstrated in a previous study, the purpose of gradient layer serves to mitigate film stress and led to improved surface roughness and Q-factor [24], [25], [26]. Throughout all three steps, a constant N₂ flow of 20 sccm was maintained, with no use of Ar as a process gas. For the 780 nm bulk AlScN layer with a 42% Sc concentration, the Al and Sc 4-inch target powers were set at 1 kW and 770 W, respectively. The Sc concentration was measured using Energy Dispersive X-ray Spectroscopy (EDS). The EDS was calibrated based on a reference sample that had been measured using Rutherford Backscattering Spectrometry (RBS). During the gradient layer deposition, the Sc target power was gradually increased from 0 to 770 W while keeping the Al target power constant. The chamber pressure remained approximately 8.0×10^{-4} mbar during deposition. After the AlScN film deposition, the films were subjected to analysis using Atomic Force Microscopy (AFM, Bruker Icon) and an X-Ray Diffractometer (XRD, Rigaku Smart Lab), as depicted in Fig. 1 (b) and (c). Omega scan data of the deposited AlScN centered at 18.3° with a Full Width at Half Maximum (FWHM) of 1.43°, indicating a high c-axis orientation of the film. This value was slightly greater than that observed in the Al_{0.6}Sc_{0.4}N grown by molecular beam epitaxy, which had a value of 0.99° [17]. AFM scans revealed a root mean square roughness (Rq) of approximately 1.31 nm across a $10 \times 10 \ \mu \text{m}^2$ area, suggesting the absence of abnormally oriented grains (AOGs) [24].

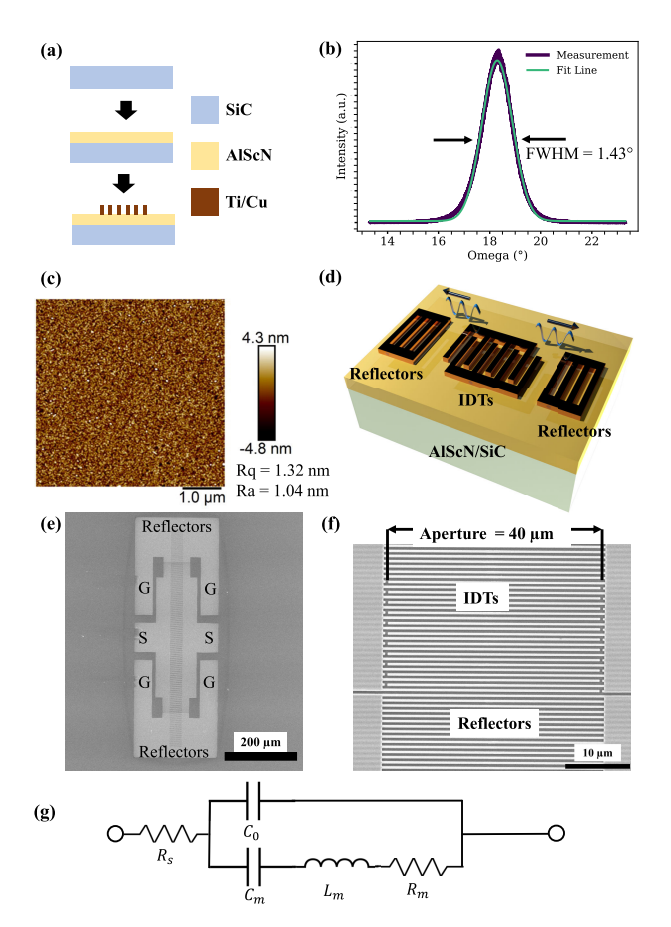


Fig. 1. (a) Process flow for fabrication of the AlScN/SiC SAW resonators (b) XRD rocking curve measurement of 830 nm AlScN on top of SiC. The Full Width at Half Maximum (FWHM) is 1.43°. (c) AFM image of $\sim\!0.8~\mu\mathrm{m}$ thick AlScN film deposited on SiC. Root mean square roughness (Rq) and average roughness (Ra) are 1.32 nm and 1.04 nm, respectively. (d) Schematic of a SAW resonator. (e) Scanning electron microscope (SEM) image of the entire SAW including IDTs and reflectors. Ground (G) and Signal (S) pads are labeled in the image. (f) SEM image focusing on the IDTs and reflectors. (g) mBVD equivalent circuit model of the SAW Resonator.

Electron beam lithography (EBL) (Elionix ELS-7500EX) was used to pattern lines with various widths and spaces for interdigital transducers (IDTs). This was followed by Ti/Cu (10 nm/170 nm) ebeam evaporation and liftoff. Fig. 1 (d) provides an overview schematic of the SAW resonators. Two Bragg mirrors positioned on both sides of the IDTs were employed as reflectors to confine the SAW. The wavelength of the SAW equaled twice the pitch of the IDTs and reflectors. Fig. 1 (d) and (e) display a Scanning Electron Microscope (SEM) image of a fabricated IDT and Bragg mirror.

The choice of copper as the top electrode material for SAW resonators is primarily due to its high electrical conductivity and, more importantly, its modal mass and stiffness characteristics. Research on leaky shear horizontal SAWs and cross-sectional Lamé mode resonators has demonstrated that dense and stiff IDT electrodes are crucial for optimal performance. There is an optimal electrode thickness for a given wavelength and electrode material, as identified in these studies [27], [28], [29], [30], [31]. The IDT contributes to shifting the stress from the piezoelectric material towards the metal electrode. As the stress moves closer to the interface

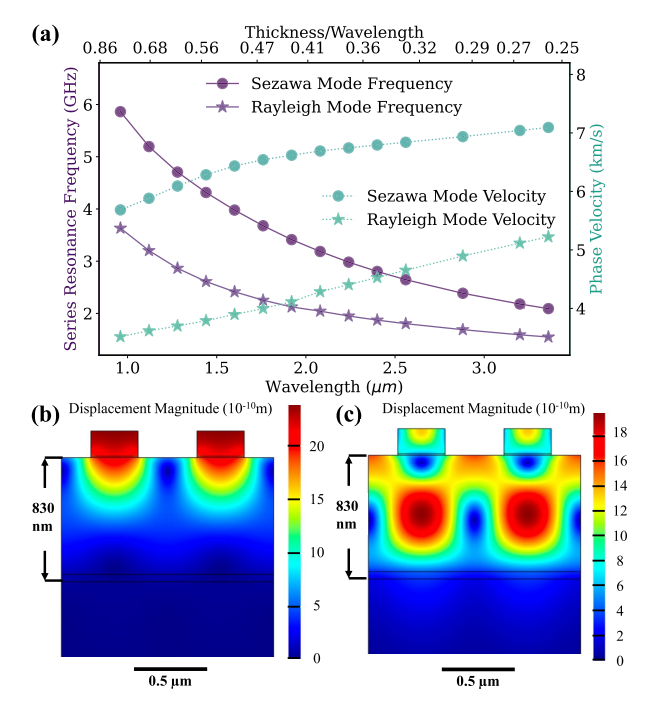


Fig. 2. (a) Measurement results showcasing the resonance frequencies (f_s) of the SAW resonators' Rayleigh modes and Sezawa modes. The dashed and solid lines are a guide to the eye. (b-c) Finite Element Method (FEM) simulations displaying the mode displacement of an 830 nm AlScN-on-SiC device equipped with 10 nm Ti and 170 nm Cu electrodes for (b) the Rayleigh mode and (c) the Sezawa mode.

between the metal and the piezoelectric layer, it better couples with the electric field, leading to an increased K² [30]. Denser and stiffer materials, such as copper, outperform aluminum in this regard. Aluminum typically requires a much larger thickness to achieve the optimal coupling coefficient, which can present fabrication challenges.

Resonator performance was measured using a Keysight vector network analyzer (VNA) P9374A with a power level of -20 dBm with $50~\Omega$ port impedances. Prior to measurement, a two-port calibration to the probe tips was performed within the desired frequency range using the Short-Open-Load-Through (SOLT) method. No de-embedding was utilized. Resonator parameters were manually extracted from the measured S-parameter data. Additionally, the widely recognized modified Butterworth Van Dyke (mBVD) circuit model allowed for further assessment of the fabricated resonators (Fig. 1 (g)).

III. MEASUREMENT AND DISCUSSION

From a resonator design perspective, understanding the relationship between the resonance frequency and the wavelength of the SAW is crucial, as it serves as a key fabrication parameter. Fig. 2 (a) shows the measured dispersion relationships of the Sezawa and Rayleigh modes of the SAW devices. The devices utilize an aperture width of 40 μ m, 125 IDT finger pairs, and 120 reflectors. The Rayleigh mode represents the fundamental mode with a frequency range spanning from 1 to 4 GHz. The Sezawa mode is the second mode at even higher frequencies, typically displaying higher K² and Q-factors when the piezoelectric layer thickness and

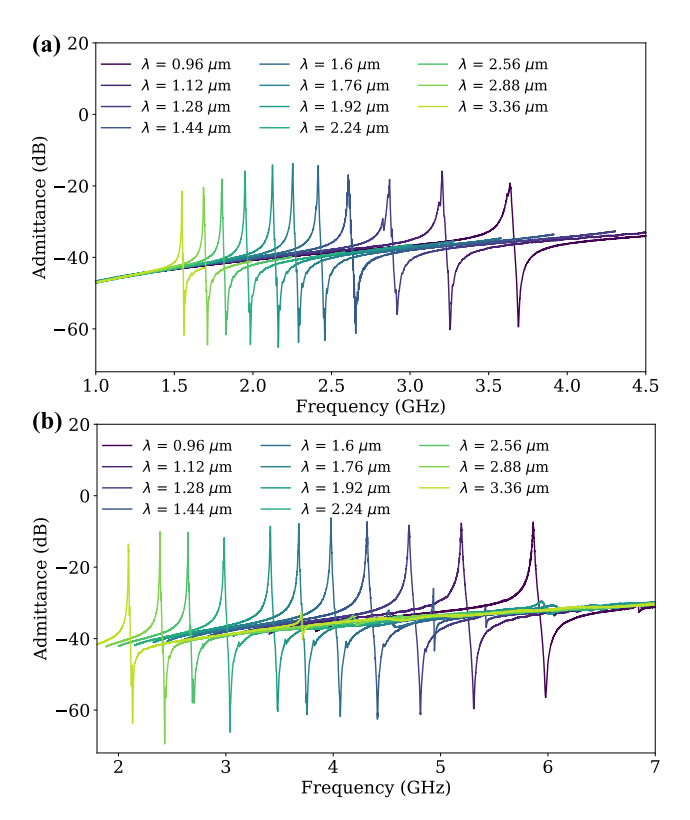


Fig. 3. (a) Admittance curves depicting the measured Rayleigh modes of the fabricated SAW resonators with varying wavelengths. (b) Admittance curves illustrating the measured Sezawa modes of the fabricated SAW resonators with differing wavelengths.

IDT design remain constant [9], [32]. Due to its substantial phase velocity, the Sezawa mode is utilized for high-frequency SAW resonator fabrication and demonstration. For simulations, COMSOL Multiphysics® version 5.6 was employed to model the SAW resonators featuring a 10 nm Ti layer and a 170 nm Cu layer atop an 830 nm AlScN on a SiC substrate. In this finite element method (FEM) simulation, an infinitely repeated IDT finger pair assumption was applied, allowing for the simulation of just one pair of IDT fingers with periodic repetition. The distinction between the Sezawa and Rayleigh modes becomes evident in the total mechanical displacement field at the resonance frequencies corresponding to the Rayleigh and Sezawa modes, as depicted in Fig. 2 (b) and (c). Specifically, the Rayleigh mode is localized near the top surface (AlScN) of the SAW resonator, whereas the Sezawa mode is confined to the interface between AlScN and SiC.

Fig. 3 (a) and (b) showcase the measured admittance response of the SAW resonators within the frequency range of 1 to 7 GHz. Fig. 2 (a) shows the measured admittances of the Rayleigh modes while Fig. 2 (b) displays the frequency response of the Sezawa modes. The resonance frequencies of both the Rayleigh modes and Sezawa modes increase as the designed wavelength of the IDT decreases, with minimal spurs observed outside the Rayleigh and Sezawa frequency band.

Fig.4 compares the measured and simulated K^2 values and f_s of the Sezawa mode for the SAW resonators. Additionally, Fig. 5 contrasts the measured and simulated K^2 values and f_s of

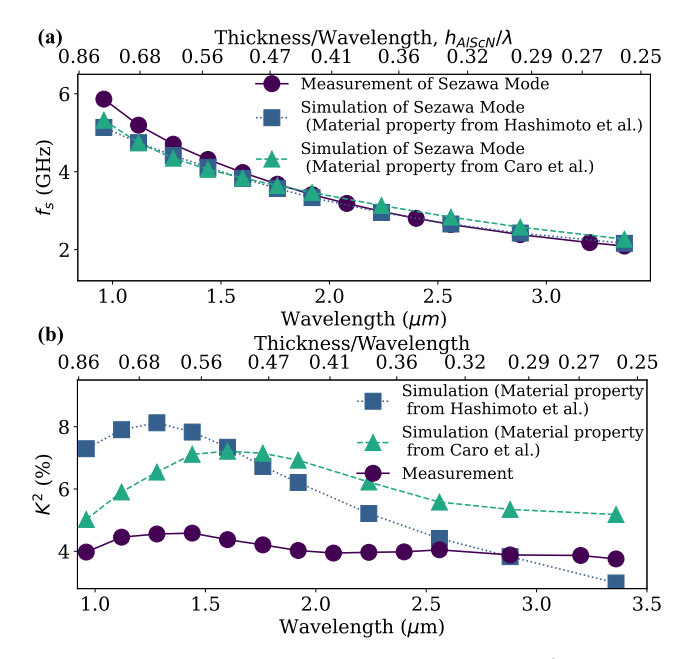


Fig. 4. (a) Comparison between measurement and COMSOL® simulation of the Sezawa mode's series resonance frequency (f_s) . (b) Comparison between measurement and COMSOL® simulation of the Sezawa mode's coupling coefficient (K^2) . COMSOL® simulations utilize the materials properties from Hashimoto et al. and Caro et al. [9], [20]. The dashed and solid lines serve as visual aids.

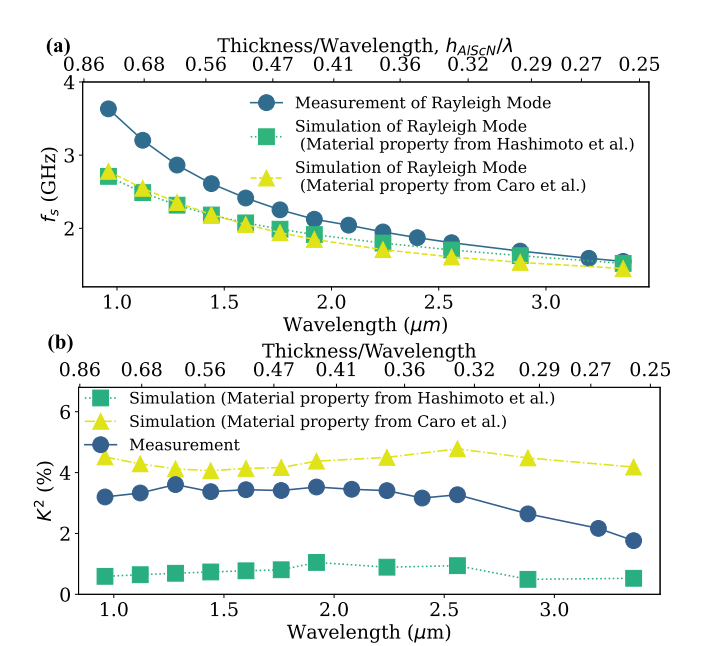


Fig. 5. (a) Comparison between measurement and COMSOL® simulation of the Rayleigh mode's series resonance frequency (f_s). (b) Comparison between measurement and COMSOL® simulation of the Rayleigh mode's coupling coefficient (K^2). COMSOL® simulations utilize the materials properties from Hashimoto et al. and Caro et al. [9], [20]. The dashed and solid lines serve as visual aids.

the Rayleigh mode SAW resonators. To account for the influence of spurs between f_s and f_p , which can cause inaccurate estimation of the Q-factor and K^2 , the measured admittance responses were fit using the mBVD circuit model and K^2 , series resonance Q-factor (Q_s) , and parallel resonance Q-factor (Q_p) were calculated from the circuit model response. The

Q-factor is defined as the frequency of the series resonance (f_s) or parallel resonance (f_p) over its 3 dB-bandwidth and the K^2 is calculated using the formula shown

$$K^2 = \frac{f_p^2 - f_s^2}{f_s^2}. (1)$$

To the best of our knowledge, there are only two sets of AlScN material parameters that have been previously proposed for Sc alloying exceeding 40%. Hashimoto et al. initially introduced the elastic constants, piezoelectric constants, and dielectric constants of 40% AlScN, alongside demonstrating the close agreement between simulated results and measurements of AlScN/6H-SiC SAW delay lines with a wavelength of 4 μ m and AlScN thickness of 2 μ m [9]. They demonstrated a frequency of 1.6 GHz and K² of 4.8% with this setup [9]. Caro et al. conducted a density functional theory (DFT) analysis of AlScN's electromechanical properties [20]. Gokhale et al. incorporated Caro et al.'s proposed material properties into their finite element simulation, comparing scenarios with wavelengths of 3, 4, and 5 μ m and AlScN thicknesses of 500 nm [11]. They demonstrated that the resonance frequency and phase velocity of the measured Sezawa modes matched those of the simulation. However, in their study, the resonance frequency and velocity of the measured Rayleigh modes exceeded those of the simulated frequency. In all, a systematic comparison between finite element simulated responses and measured responses is still lacking, particularly at high frequencies (> 3 GHz) and small wavelengths ($< 3 \mu m$).

As depicted in Fig. 4 (a), the simulated Sezawa mode frequency closely aligns with the measured data. A f_s of 5.9 GHz was attained with a wavelength of 0.96 μ m. The phase velocity, which is the product of wavelength and resonance frequency, demonstrates an increase with wavelength. This phenomenon occurs because at longer wavelengths, the velocity rises due to greater coupling of the surface acoustic Sezawa mode into the SiC substrate, where the sound velocity of 4H-SiC (11,900 m/s) exceeds that of AlScN [33]. As a result, a maximum Sezawa velocity of 7,100 m/s was achieved at wavelength of 3.36 μ m.

Due to the mass loading effect, Tang et al. demonstrated that employing copper electrodes in IDT materials could elevate the K² from 2.8% to 9.1% for the AlScN/Si structure, showcasing a much greater improvement compared to aluminum electrodes, which can achieve a maximum of 7.7%. They also illustrated that the coupling coefficient peaks when the ratio of copper electrode thickness to wavelength is approximately 0.15 [34]. This corresponds with our findings, as depicted in Fig. 4 and 5. K² reaches its maximum at a wavelength of 1.44 μ m and a copper thickness of 170 nm, resulting in a thickness-to-wavelength ratio of 0.12. The electrode thickness-to-wavelength ratio of other frequencies have not been optimized in this study. Future studies can maintain a constant ratio of 0.12 for all the different wavelengths SAW devices, potentially enhancing K² across the entire frequency range. Additionally, using metals with higher acoustic impedance, such as tungsten, which have greater Young's modulus and density, could further improve overall K² [30], [31].

The maximum of 8% achieved in the simulation is almost two times higher than the measured K^2 , as shown in Fig. 4. This discrepancy is likely due to the limited reflectivity of the Bragg mirror which stores significant acoustic energy, which will be further addressed below.

With an aperture width of 40 μ m, 125 IDT finger pairs, and 120 reflectors, the measured Sezawa mode's K² reaches a maximum of 4.6% at 4.3 GHz and a wavelength of 1.44 μ m, corresponding to an AlScN thickness/wavelength ratio (t/ λ) of 0.58. Across the wavelength range of 0.96 μ m to 2.56 μ m, where f_s ranges from 5.9 GHz to 2.6 GHz, the K² maintains a value greater than 3.5%, consistent with some previous reports. Hashimoto et al. reported a simulated maximum of 5.26% at t/ λ = 0.58 for Al_{0.58}Sc_{0.42}N/SiC [9], while Gokhale et al. reported a simulated maximum of 2.5% at t/ λ = 0.35 for Al_{0.75}Sc_{0.25}N/SiC [11].

The resonance frequency of the measured Rayleigh mode surpasses that of the simulation, and both Hashimoto's and Caro's material properties indicate comparable velocities. However, there is notable difference between Hashimoto's and Caro's materials properties in the simulated K^2 , due to their difference in the elastic constant and piezoelectric constants, whereas the measured value of K^2 falls between the two simulations. A maximum of 3.6% for K^2 was achieved at a wavelength of 1.28 μ m and f_8 of 2.9 GHz.

The Q-factor obtained may be influenced by both the reflectivity of copper, which can vary with the SAW wavelength, and the inherent loss of the AlScN piezoelectric material. The copper mirrors might confine energy differently at different wavelengths, leading to varying Q-factors. Investigating the characteristics of the device, it has been observed that both the Rayleigh mode and Sezawa mode showed high Q-factor (>200). In the Sezawa mode, the Q_s reaches its maximum of 702 at 3.2 GHz and its minimum of 297 at 2.1 GHz. The Q_p achieves its maximum of 781 at 3.2 GHz and a minimum of 331 at 2.1 GHz. These devices typically have a series resistance, R_s , of around $1\sim 2$ Ω . To investigate the impact of R_s, a reference short device was fabricated where the IDT finger pairs and mirrors were replaced with a sheet of metal. According to the admittance measurement, this device is equivalent to a 0.1 Ω resistor in series with a 0.45 nH inductor. This indicates that most of the series' resistance originates from the IDT finger pairs themselves. Therefore, de-embedding this small resistance will not be helpful in improving the overall device Q_s . Other techniques which reduce the resistance of the IDT fingers, for instance, decreasing the entire SAW aperture or increasing the metal thickness, can be used to enhance the overall Q_s .

An analysis was conducted on the impact of both the number of IDT fingers and the number of reflectors to delve into the disparity observed between the simulated and measured K^2 values. SAW resonators featuring varying numbers of IDT finger pairs were fabricated and compared in Fig. 6. These devices were designed with an aperture width of 40 μ m and 100 reflectors, corresponding to a wavelength of 1.44 μ m and a resonance frequency of approximately 4.3 GHz. As the

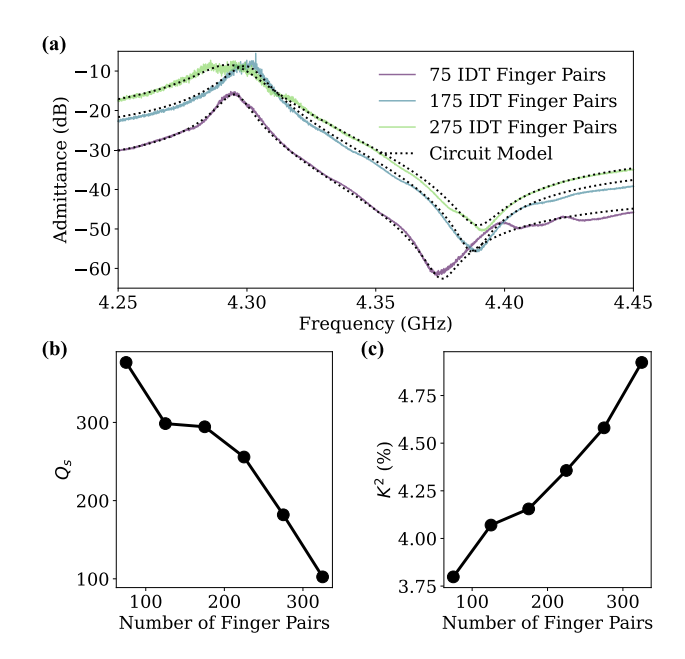


Fig. 6. (a) Comparative analysis of measured admittance responses based on varying numbers of IDT finger pairs. (b) Comparison of the series resonance Q-factor (Q_s) with varying numbers of IDT finger pairs. (c) Comparison of the coupling coefficient (K^2) values concerning different number of IDT finger pairs.

number of IDT finger pairs increased, the admittance response shifted upward to smaller impedances due to the rise in parallel capacitance (C_0). As the number of IDT finger pairs increases to 325, the motional impedance, R_m , decreases. Consequently, the series resonance peak broadens, leading to a decrease in Q_s . The admittance response fluctuates around the series resonance peak as the impedance reaches a very low value, underscoring the importance of determining the Q-factor and K^2 from the circuit model fitting as indicated by the dotted line. K^2 increased from 3.8% to 4.9% with the number of IDT finger pairs. However, this improvement came at the cost of reduced Q_s , which decreased from 377 to 102 when compared to other 4.3 GHz devices.

One reference open device without IDT fingers and mirrors but with the same pad design as the SAW with 40 μ m aperture, 125 IDT finger pairs, and 120 reflectors has been fabricated and measured. According to the admittance measurement, the pad-to-pad feedthrough capacitance is 0.02 pF. This capacitance is significantly smaller than the capacitance within the IDT. Thus, the improvement in K^2 with increasing IDT pairs does not originate from an increase in the IDT capacitance with respect to that between the pads. Instead, the enhancement in K² is due to the increased area of the IDT coupling regions relative to the mirror regions. The increase in K² with more IDT finger pairs indicates that expanding the coupling region while maintaining the same mirror results in more of the total mechanical energy being stored within the IDT. Surface acoustic wave energy is stored in both the IDT regions and mirror regions. However, the energy stored in the mirror decreases K^2 , because it is not readily available for transducer. Consequently, with a larger area of IDTs, the measured K² improved. This serves as one of the reasons for the lower simulated K² compared to the measured K². Future

studies utilizing reflector materials with higher reflectivity than copper, for example, tungsten, could maintain the same Q-factor while improving K^2 by better confining the SAW energy in the IDT region.

By comparing the C_0 of SAW resonators with different number of IDTs finger pairs, the permittivity of $Al_{0.58}Sc_{0.42}N$ can also be calculated. The parallel capacitance obtained by circuit model fitting are 0.42 pF, 0.75 pF, 1.12pF, 1.3 pF, and 1.68 pF for SAW resonators with 75, 125, 175, 225, 275 finger pairs, respectively. This corresponds to approximately 0.15 nF capacitance per meter per finger pair. A previous study has shown that when the thickness-to-wavelength ratio exceeds 0.08, the electric field strength decays exponentially along the thickness, and the permittivity of the regions nearest to the surface have a greater influence on the measured capacitance than those further away. In such cases, the IDT fingers can no longer be considered as a parallel plate capacitor [35]. Instead, the elliptical integral of electric field must be adapted to calculate the C_0

$$C_0 = \epsilon_0 \epsilon_{eff} \frac{K(k_0')}{K(k_0)} L_e N_p \tag{2}$$

where N_p represents the pairs of IDTs, L_e stands for the acoustic aperture, ε_0 denotes the permittivity of vacuum, K(k) is the complete elliptic integral of the first kind, and k_0 is the modulus of the elliptic integral function. The detailed equation for k_0 and effective permittivity ϵ_{eff} can be found in [36]. For this device, the wavelength is 1.44 μ m, the thickness of AlScN is 830 nm, and both the electrode width and gap are 0.36 μ m. Using the capacitance density of 0.15 nF capacitance per meter per finger pair, the ϵ_{eff} can be calculated as 13.2. Given the relative permittivity of 4H-SiC is 9.7 [37], the relative permittivity of $Al_{0.58}Sc_{0.42}N$ can be found as 29. This is consistent with the value reported by Hashimoto of 30 [9].

Fig. 7 illustrates a scenario where the spurs overlap with fp, invalidating the direct 3dB bandwidth Q-factor calculation from the measured response. This spurious mode is known as the transverse mode. Although both devices operate with similar frequency around 2.5 GHz, the Sezawa mode depicted in Fig. 7 (d-f) operates at a significantly higher velocity than the Rayleigh mode in Fig. 7 (a-c). This leads to a smaller frequency spacing in the Rayleigh mode (Fig. 7 a-c) than in the Sezawa mode (Fig. 7 d-f). The scenario is depicted where spurs overlap with f_p, rendering the direct 3dB bandwidth Q-factor calculation from the measured response invalid. For devices operating at frequencies above 4 GHz, the spurious modes are less prominent, possibly due to the larger effective aperture. Several techniques have been introduced previously to suppress these transverse modes, such as apodization IDT [38], piston mode IDT [39], and tilted IDT [40].

Another method to evaluate Q-factor involves using the Bode Q (Q_{max}), which is defined by using the phase group delay of the S_{11} , as expressed in (3).

$$Q_{Bode} = \omega \frac{d\phi}{d\omega} \frac{|S_{11}|}{1 - |S_{11}|^2}.$$
 (3)

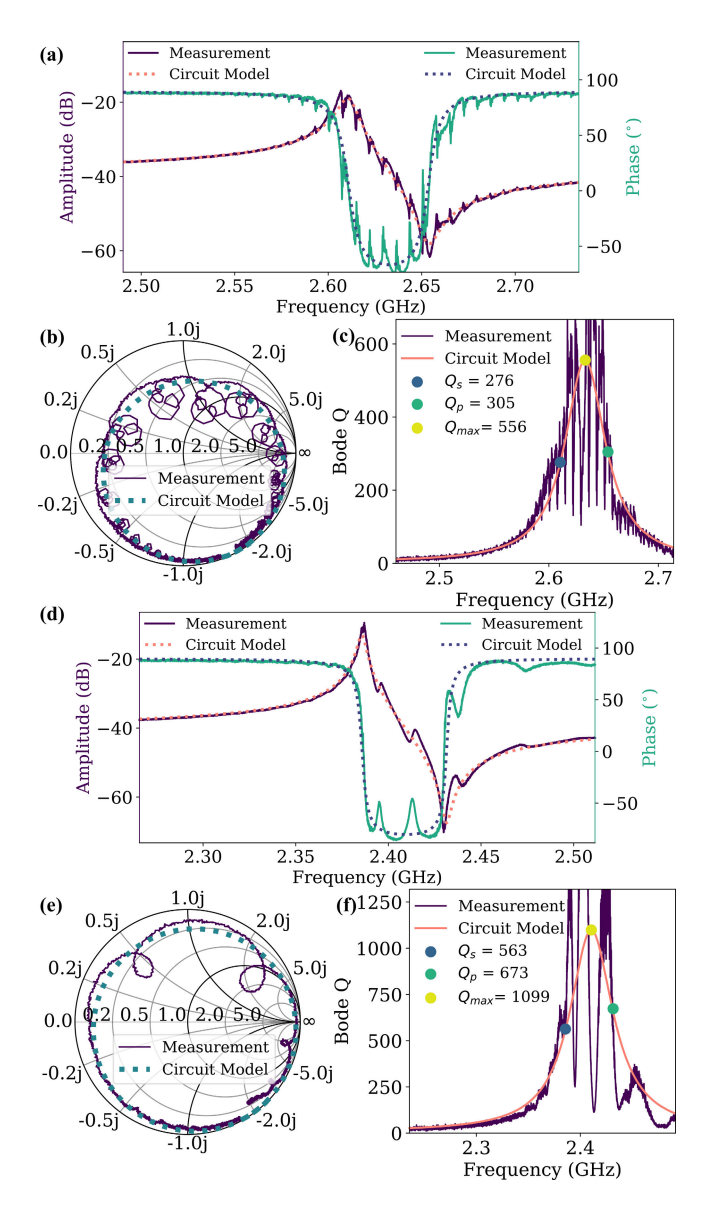


Fig. 7. Admittance response (a and d), Smith plot with 50 Ω reference impedance (b and e), Q_{max} with changed source impedance (c and f) for (a-c) Rayleigh mode with wavelength of 1.28 μ m and (b-f) Sezawa mode with wavelength of 2.88 μ m.

Here $\frac{d\phi}{d\omega}$ represents the group delay of the S₁₁ measurement of the resonator, where Φ represents the phase of S_{11} and ω denotes the radial frequency. In order to calculate Q_{max} of the SAW resonators, all of the S-parameter data must lie nearly equidistant from the center of the Smith chart [22], [41]. As depicted in Fig. 7 (b and e), a 50 Ω source impedance is not sufficient to center the Smith chart. Therefore, source impedances of 80.1-15.7j and 91.7-6.6j were selected to calculate the Bode Q in Fig. 7 (c) and (f), respectively. The Q_s and Q_p are annotated in the figure, and they align on the same line on both the Bode Q of the measurements and the Bode Q circuit model. This illustrates the effectiveness of the circuit model fitting and Bode Q calculation. The oscillation between f_s and f_p is attributed to the transverse mode, and the circuit model fitting aids in filtering out those spurious modes and determining the accurate value.

Fig. 8 (a, b, and e) shows the measured response of four different SAW resonators with frequencies ranging

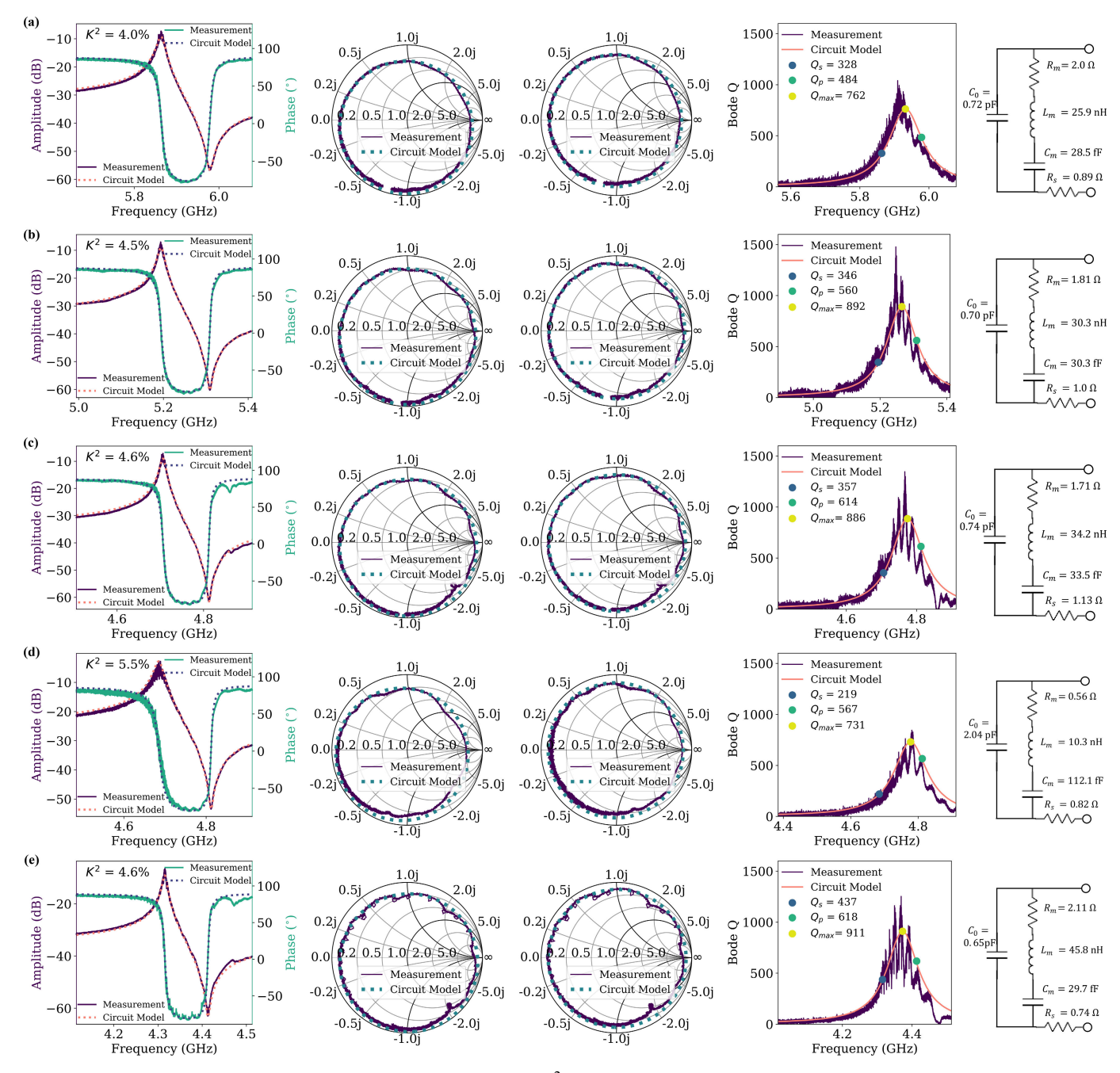


Fig. 8. From left to right: Admittance response (with coupling coefficient (K^2) labeled), Smith plot with 50 Ω reference impedance, Smith plot with modified reference impedance, Bode Q with modified impedance, and circuit model of Sezawa mode SAW resonators with wavelength of (a) 0.96 μ m, (b) 1.12 μ m, (c-d) 1.28 μ m, and (e) 1.44 μ m. (a,b,c, and e) SAW resonator with aperture of 40 μ m, 125 IDT finger pairs, and 120 reflectors. (d) SAW resonator with aperture of 40 μ m, 350 IDT finger pairs, and 120 reflectors. The changed port impedances are (a) 48.2-4.9j Ω , (b) 50-4.1j Ω , (c) 52.2- 3.5j Ω , (d) 28.1- 1.7j Ω , and (e) 57.3- 3.7j Ω .

from $4{\sim}6$ GHz, demonstrating the high K^2 and Q-factor of the fabricated devices. The devices were designed with an aperture width of 40 μm , 125 IDT finger pairs, and 120 reflectors and with different wavelengths from 0.96 μm and 1.44 μm . The circuit model showed a good agreement with the measured frequency response. All four resonators exhibit an R_s of around 1 Ω and C_0 of around 0.7 pF. Fig. 8 (c) illustrates another scenario where more IDT finger pairs were added to enhance K^2 at the cost of reduced Q- factor, resulting in a K^2 increase from 4.6% to 5.5%.

IV. CONCLUSION

Table I provides a comparison of the SAW resonators with state-of-the-art high-frequency SAW counterparts from the literature. The Figure of Merit (FoM) defined as the $K^2 \times Q_p$, reaches a peak value of 31 at a frequency of 4.7 GHz in the resonator devices. This FoM value is more than double that of previous works utilizing AlScN to form SAW resonators. In this study, a maximum resonance frequency of 5.9 GHz was achieved, surpassing the previously highest frequency of 4.61 GHz achieved for AlScN based SAW resonators. Recent research has showcased leaky SAW resonators using LiNbO₃

TABLE I
COMPARISON OF HIGH FREQUENCY ALSCN SURFACE
ACOUSTIC WAVE RESONATORS

Year	Material	Freq (GHz)	K ²	Qs	Qp	FoM	Qmax
This work	Al _{0.58} Sc _{0.42} N / SiC	5.9	4.0%	328	484	19	762
		5.2	4.5%	346	560	25	892
		4.7	4.6%	357	614	28	886
		4.7	5.5%	219	567	31	731
		4.3	4.6%	437	618	28	911
2024	X cut	4.9	34%	-	-	-	650
[42]	LiNbO ₃ /SiC	5.9	26%	-	-	-	300
2023 [5]	X cut LiNbO ₃ /SiC	4.95	15.9%	-	-	-	408
2023 [6]	Al _{0.66} Sc _{0.34} N/ Diamond	3.71	6.3%	120	23	7.6	ı
	Al _{0.57} Sc _{0.43} N/ Diamond	3.73	5.4%	311	22	16.6	1
2022 [46]	Al _{0.8} Sc _{0.2} N/ GaN/ Sapphire	4.61	ı	I	ı	-	571
2020 [11]	Al _{0.75} Sc _{0.25} N/ SiC	3.73	0.5%	Ī	108	0.6	
2019 [23]	$\begin{array}{c} Al_{0.88}Sc_{0.12}N/\\ Si\end{array}$	3.6	3.0%	-	146	5.4	_
2013 [9]	Al _{0.6} Sc _{0.4} N/ SiC	3.8	4.5%	340	240	15.3	_

on SiC, achieving remarkably high K² at 4.9-5.9 GHz [5]. Although the acoustic energy is well confined in the LiNbO₃ at the resonant frequency, Zheng et al. utilized 2D FEM to show that partial acoustic energy leaks into the substrate at the parallel resonance frequency, which results in a moderate Q_p [5]. Furthermore, some of these studies employed narrow (150 nm) and thin gold electrodes, which exhibited high series resistance and consequently constrained the Q_s [42]. It is also noteworthy that AlScN/SiC based SAW resonators offer several advantages over LiNbO₃/SiC based SAW resonators. In this study, AlScN could be directly sputtered on top of SiC, simplifying the fabrication process and reducing costs. In contrast, LiNbO₃ thin films require complex steps such as ion implantation, exfoliation, transferring, post-annealing, and chemical-mechanical polishing for integration with SiC [5], [43]. Additionally, AlScN/SiC based SAW devices are suitable for applications requiring high temperatures or integration with processes requiring elevated temperatures. The high pyroelectric coefficient of LiNbO₃ renders it vulnerable to shattering under rapid temperature changes [44], [45].

In conclusion, we successfully demonstrated high-performance SAW resonators utilizing a sputtered Al_{0.58}Sc_{0.42}N-on-SiC platform, optimized for high frequency, high K², high Q-factor, and weak spurious modes. We attribute this to the exceptional piezoelectric properties of the AlScN thin films and the lattice matching of the SiC substrate. The impact of varying IDT finger pairs on performance was thoroughly explored. The frequency response trends concerning different wavelengths and frequencies were also

outlined. Our devices outperform previous high-frequency SAW devices using AlScN due to the SiC substrate's higher acoustic velocity and better lattice matching to AlScN, the co-sputtering process optimizing AlScN film quality [25], and the structural optimizations including a thick copper electrode improving the coupling coefficient. While further optimization of IDT finger geometry is required to address spurious modes in the low-frequency SAW resonators, this study underscores the promising potential of AlScN/SiC acoustic devices for radio-frequency applications.

REFERENCES

- C. C. W. Ruppel, "Acoustic wave filter technology—A review," *IEEE Trans. Ultrason., Ferroelect., Freq. Control*, vol. 64, no. 9, pp. 1390–1400, Sep. 2017, doi: 10.1109/TUFFC.2017.2690905.
- [2] Y. Liu, Y. Cai, Y. Zhang, A. Tovstopyat, S. Liu, and C. Sun, "Materials, design, and characteristics of bulk acoustic wave resonator: A review," *Micromachines*, vol. 11, no. 7, p. 630, Jun. 2020, doi: 10.3390/mi11070630.
- [3] S. Elisabeth and C. Malaquin, "Intensifying technology competition in the acoustic wave filter market," *Microw. J.*, vol. 63, no. 10, pp. 20–30, 2020
- [4] M. Fiagbenu et al., "A K-band bulk acoustic wave resonator using periodically poled Al_{0.72}Sc_{0.28}N," *IEEE Electron Device Lett.*, vol. 44, no. 7, pp. 1196–1199, Jul. 2023, doi: 10.1109/LED.2023.3282170.
- [5] P. Zheng et al., "Near 5-GHz longitudinal leaky surface acoustic wave devices on LiNbO₃/SiC substrates," *IEEE Trans. Microw. Theory Techn.*, vol. 72, no. 3, pp. 1480–1488, Mar. 2024.
- [6] K. Hatashita et al., "High electro-mechanical coupling coefficient SAW device with ScAlN on diamond," *Jpn. J. Appl. Phys.*, vol. 62, no. 2, Feb. 2023, Art. no. 021003.
- [7] L. Lei, B. Dong, Y. Hu, Y. Lei, Z. Wang, and S. Ruan, "High-frequency surface acoustic wave resonator with diamond/AlN/IDT/AlN/diamond multilayer structure," *Sensors*, vol. 22, no. 17, p. 6479, Aug. 2022, doi: 10.3390/s22176479.
- [8] S. Valle, M. Singh, M. J. Cryan, M. Kuball, and K. C. Balram, "High frequency guided mode resonances in mass-loaded, thin film gallium nitride surface acoustic wave devices," *Appl. Phys. Lett.*, vol. 115, no. 21, Nov. 2019, Art. no. 212104.
- [9] K.-Y. Hashimoto, S. Sato, A. Teshigahara, T. Nakamura, and K. Kano, "High-performance surface acoustic wave resonators in the 1 to 3 GHz range using a ScAlN/6H-SiC structure," *IEEE Trans. Ultrason.*, Ferroelectr., Freq. Control, vol. 60, no. 3, pp. 637–642, Mar. 2013.
- [10] X. Du, Z. Tang, C. Leblanc, D. Jariwala, and R. H. Olsson, "High-performance SAW resonators at 3 GHz using AlScN on a 4H-SiC substrate," in *Proc. Joint Conf. Eur. Freq. Time Forum IEEE Int. Freq. Control Symp.* (EFTF/IFCS), Apr. 2022, pp. 1–2.
- [11] V. J. Gokhale, B. P. Downey, M. T. Hardy, E. N. Jin, J. A. Roussos, and D. J. Meyer, "Epitaxial single-crystal ScAlN on 4H-SiC for high-velocity, low-loss SAW devices," in *Proc. IEEE 33rd Int. Conf. Micro Electro Mech. Syst. (MEMS)*, Jan. 2020, pp. 1262–1265, doi: 10.1109/MEMS46641.2020.9056271.
- [12] M. E. Levinshtein, S. L. Rumyantsev, and M. S. Shur, Properties of Advanced Semiconductor Materials: GaN, AIN, InN, BN, SiC, SiGe. Hoboken, NJ, USA: Wiley, 2001.
- [13] J. Shen et al., "SAW filters with excellent temperature stability and high power handling using LiTaO₃/SiC bonded wafers," *J. Microelectromech.* Syst., vol. 31, no. 2, pp. 186–193, Apr. 2022.
- [14] L. Hackett et al., "S-band acoustoelectric amplifier in an InGaAs-AlScN-SiC architecture," Appl. Phys. Lett., vol. 124, no. 11, Mar. 2024, Art. no. 113503.
- [15] Y. He et al., "Metal-ferroelectric AlScN-semiconductor memory devices on SiC wafers," *Appl. Phys. Lett.*, vol. 123, no. 12, Sep. 2023, Art. no. 122901, doi: 10.1063/5.0161746.
- [16] R. D. Felice, J. E. Northrup, and J. Neugebauer, "Energetics of AlN thin films and the implications for epitaxial growth on SiC," *Phys. Rev. B*, *Condens. Matter*, vol. 54, no. 24, pp. R17351–R17354, Dec. 1996.
- [17] M. T. Hardy et al., "Nucleation control of high crystal quality heteroepitaxial Sc_{0.4}Al_{0.6}N grown by molecular beam epitaxy," *J. Appl. Phys.*, vol. 134, no. 10, Sep. 2023, Art. no. 105301.

- [18] O. Zywitzki et al., "Effect of scandium content on structure and piezoelectric properties of AlScN films deposited by reactive pulse magnetron sputtering," Surf. Coatings Technol., vol. 309, pp. 417–422, Jan. 2017, doi: 10.1016/j.surfcoat.2016.11.083.
- [19] M. Akiyama, K. Umeda, A. Honda, and T. Nagase, "Influence of scandium concentration on power generation figure of merit of scandium aluminum nitride thin films," *Appl. Phys. Lett.*, vol. 102, no. 2, Jan. 2013, Art. no. 021915, doi: 10.1063/1.4788728.
- [20] M. A. Caro et al., "Piezoelectric coefficients and spontaneous polarization of ScAlN," J. Phys., Condens. Matter, vol. 27, no. 24, Jun. 2015, Art. no. 245901.
- [21] R. H. Olsson, Z. Tang, and M. D'Agati, "Doping of aluminum nitride and the impact on thin film piezoelectric and ferroelectric device performance," in *Proc. IEEE Custom Integr. Circuits Conf. (CICC)*, Mar. 2020, pp. 1–6.
- [22] D. A. Feld, R. Parker, R. Ruby, P. Bradley, and S. Dong, "After 60 years: A new formula for computing quality factor is warranted," in *Proc. IEEE Ultrason. Symp.*, Nov. 2008, pp. 431–436.
- [23] Z. Hao et al., "Single crystalline ScAlN surface acoustic wave resonators with large figure of merit (Q × k_I²)," in *IEEE MTT-S Int. Microw. Symp. Dig.*, Jun. 2019, pp. 786–789.
- [24] R. Beaucejour, M. D'Agati, K. Kalyan, and R. H. Olsson, "Compensation of the stress gradient in physical vapor deposited Al_{1-x}ScxN films for microelectromechanical systems with low out-of-plane bending," *Micromachines*, vol. 13, no. 8, p. 1169, Jul. 2022.
- [25] R. Beaucejour, V. Roebisch, A. Kochhar, C. G. Moe, M. D. Hodge, and R. H. Olsson, "Controlling residual stress and suppression of anomalous grains in aluminum scandium nitride films grown directly on silicon," *J. Microelectromech. Syst.*, vol. 31, no. 4, pp. 604–611, Aug. 2022.
- [26] C. M. Flannery and H. von Kiedrowski, "Effects of surface roughness on surface acoustic wave propagation in semiconductor materials," *Ultrasonics*, vol. 40, nos. 1–8, pp. 83–87, May 2002.
- [27] K. Hashimoto, H. Asano, K. Matsuda, N. Yokoyama, T. Omori, and M. Yamaguchi, "Wideband love wave filters operating in GHz range on Cu-grating/rotated-YX-LiNbO₃-substrate structure," in *Proc. IEEE Ultrason. Symp.*, Nov. 2004, pp. 227–231.
- [28] M. Solal et al., "Existence of harmonic metal thickness mode propagation for longitudinal leaky waves," in *Proc. IEEE Ultrason. Symp.*, Aug. 2004, pp. 1207–1212.
- [29] V. Plessky, T. Makkonen, and M. M. Salomaa, "Leaky SAW in an isotropic substrate with thick electrodes," in *Proc. IEEE Ultrason.* Symp. Int. Symp., Sep. 2001, pp. 239–242.
- [30] Z. A. Schaffer, G. Piazza, S. Mishin, and Y. Oshmyansky, "Super high frequency simple process flow cross-sectional Lamé mode resonators in 20% scandium-doped aluminum nitride," in *Proc. IEEE 33rd Int. Conf. Micro Electro Mech. Syst. (MEMS)*, Jan. 2020, pp. 1281–1284.
- [31] G. Giribaldi, L. Colombo, F. Bersano, C. Cassella, and M. Rinaldi, "Investigation on the impact of scandium-doping on the k_t^2 of $ScxAl_{1-x}N$ cross-sectional Lamé mode resonators," in *Proc. IEEE Int. Ultrason. Symp. (IUS)*, Sep. 2020, pp. 1–4.

- [32] F. Hadj-Larbi and R. Serhane, "Sezawa SAW devices: Review of numerical-experimental studies and recent applications," Sens. Actuators A, Phys., vol. 292, pp. 169–197, Jun. 2019.
- [33] Y. Long, Z. Liu, and F. Ayazi, "4H-silicon carbide as an acoustic material for MEMS," *IEEE Trans. Ultrason., Ferroelectr., Freq. Control*, vol. 70, no. 10, pp. 1189–1200, 2023, doi: 10.1109/TUFFC.2023.3282920.
- [34] G. Tang, T. Han, A. Teshigahara, T. Iwaki, and K.-Y. Hashimoto, "Enhancement of effective electromechanical coupling factor by mass loading in layered surface acoustic wave device structures," *Jpn. J. Appl. Phys.*, vol. 55, no. 7S1, Jul. 2016, Art. no. 07KD07.
- [35] L. Colombo, A. Kochhar, G. Vidal-Álvarez, P. Simeoni, U. Soysal, and G. Piazza, "Sub-GHz X-cut lithium niobate S0 mode MEMS resonators," *J. Microelectromech. Syst.*, vol. 31, no. 6, pp. 888–900, Dec. 2022.
- [36] A. A. Nassr, W. H. Ahmed, and W. W. El-Dakhakhni, "Coplanar capacitance sensors for detecting water intrusion in composite structures," *Meas. Sci. Technol.*, vol. 19, no. 7, Jul. 2008, Art. no. 075702.
- [37] M. K. Kazimierczuk, Pulse-Width Modulated DC-DC Power Converters. Hoboken, NJ, USA: Wiley, 2015.
- [38] S. Matsuda, M. Miura, T. Matsuda, M. Ueda, Y. Satoh, and K.-Y. Hashimoto, "Experimental studies of quality factor deterioration in shear-horizontal-type surface acoustic wave resonators caused by apodization of interdigital transducer," *Jpn. J. Appl. Phys.*, vol. 50, no. 7S, Jul. 2011. Art. no. 07HD14.
- [39] J. Zou, J. Liu, G. Tang, C.-M. Lin, and C. S. Lam, "Transverse mode suppression in the AlN Lamb wave resonators by 'piston mode," in *Proc. IEEE Int. Ultrason. Symp. (IUS)*, Sep. 2017, pp. 1–4.
- [40] S. Wu, F. Bao, F. Xu, J. Zou, M. Li, and G. Tang, "Tilted interdigital-transducer in NS-SAW resonator for transverse mode suppression," in *Proc. Joint Conf. Eur. Freq. Time Forum IEEE Int. Freq. Control Symp. (EFTF/IFCS)*, Apr. 2022, pp. 1–4.
- [41] M. Park, Z. Hao, R. Dargis, A. Clark, and A. Ansari, "Epitaxial aluminum scandium nitride super high frequency acoustic resonators," *J. Microelectromech. Syst.*, vol. 29, no. 4, pp. 490–498, Aug. 2020.
- [42] Z. Dai, H. Cheng, S. Xiao, H. Sun, and C. Zuo, "Coupled shear SAW resonator with high electromechanical coupling coefficient of 34% using X-cut LiNbO₃-on-SiC substrate," *IEEE Electron Device Lett.*, vol. 45, no. 4, pp. 720–723, Apr. 2024.
- [43] S. Zhang et al., "Surface acoustic wave devices using lithium niobate on silicon carbide," *IEEE Trans. Microw. Theory Techn.*, vol. 68, no. 9, pp. 3653–3666, Sep. 2020.
- [44] COMSOL Multiphysics® V. 6.6. Accessed: Jun. 1, 2021. [Online]. Available: https://www.comsol.com/release/6.0
- [45] N. Kurz et al., "Temperature dependence of the pyroelectric coefficient of AlScN thin films," *Phys. Status Solidi A*, vol. 215, no. 13, 2018, Art. no. 1700831.
- [46] Y. Zheng et al., "High-order Sezawa mode AlScN/GaN/sapphire surface acoustic wave resonators," in *Proc. IEEE 35th Int. Conf. Micro Electro Mech. Syst. Conf. (MEMS)*, Jan. 2022, pp. 1046–1049.